

Lawrence Berkeley National Laboratory

LBL Publications

Title

Spectral control via multi-species effects in PW-class laser-ion acceleration

Permalink

<https://escholarship.org/uc/item/3hb941gn>

Journal

Plasma Physics and Controlled Fusion, 62(12)

ISSN

0741-3335

Authors

Huebl, Axel
Rehwald, Martin
Obst-Huebl, Lieselotte
[et al.](#)

Publication Date

2020-12-01

DOI

10.1088/1361-6587/abbe33

Copyright Information

This work is made available under the terms of a Creative Commons Attribution License, available at <https://creativecommons.org/licenses/by/4.0/>

Peer reviewed

PAPER • OPEN ACCESS

Spectral control via multi-species effects in PW-class laser-ion acceleration

To cite this article: Axel Huebl *et al* 2020 *Plasma Phys. Control. Fusion* **62** 124003

View the [article online](#) for updates and enhancements.



IOP | ebooks™

Bringing together innovative digital publishing with leading authors from the global scientific community.

Start exploring the collection—download the first chapter of every title for free.

Spectral control via multi-species effects in PW-class laser-ion acceleration

Axel Huebl^{1,2,3} , Martin Rehwald^{1,2} , Lieselotte Obst-Huebl^{1,2,4} , Tim Ziegler^{1,2} , Marco Garten^{1,2} , René Widera¹ , Karl Zeil¹ , Thomas E Cowan^{1,2} , Michael Bussmann^{1,5} , Ulrich Schramm^{1,2}  and Thomas Kluge¹ 

¹ Helmholtz-Zentrum Dresden—Rossendorf, 01328 Dresden, Germany

² Technical University Dresden, 01062 Dresden, Germany

E-mail: axelhuebl@lbl.gov

Received 12 May 2020, revised 11 September 2020

Accepted for publication 5 October 2020

Published 29 October 2020



CrossMark

Abstract

Laser-ion acceleration with ultra-short pulse, petawatt-class lasers is dominated by non-thermal, intra-pulse plasma dynamics. The presence of multiple ion species or multiple charge states in targets leads to characteristic modulations and even mono-energetic features, depending on the choice of target material. As spectral signatures of generated ion beams are frequently used to characterize underlying acceleration mechanisms, thermal, multi-fluid descriptions require revision for predictive capabilities and control in next-generation particle beam sources. We present an analytical model with explicit inter-species interactions, supported by extensive *ab initio* simulations. This enables us to derive important ensemble properties from the spectral distribution resulting from these multi-species effects for arbitrary mixtures. We further propose a potential experimental implementation with a novel cryogenic target, delivering jets with variable mixtures of hydrogen and deuterium. Free from contaminants and without strong influence of hardly controllable processes such as ionization dynamics, this would allow a systematic realization of our predictions for the multi-species effect.

Keywords: LPA, laser-ion acceleration, target-normal sheath acceleration, multi-species, cryogenic target, particle-in-cell

(Some figures may appear in colour only in the online journal)

Introduction

High-repetition-rate ultra-short pulse laser-driven ion sources are receiving increased attention due to their potential as

compact particle accelerators [1–3]. With the ascent of ultra-short pulse (< 100 fs) ultra-high intensity lasers, traditional assumptions for ambipolar ion acceleration in thermal, fluid-like conditions need revision due to the increasing influence of intra-pulse, pre-thermal dynamics [4–8]. Ion energy spectra are all the more a central observable for experiments and modeling efforts alike, as their shape and maximum energy are characteristic for acceleration mechanisms at given laser and target conditions [9–13]. Also, energy spectra are well accessible experimentally and controlling the spectral shape is important for applications [14–16].

Assuming a single ion charge-state in a target, typical target-normal sheath acceleration (TNSA) ion spectra follow an exponential distribution [2, 6]. Under ideal conditions, light-sail radiation pressure acceleration (RPA) signatures are predicted with a clear spectral gap, and a single

³ Current address: Lawrence Berkeley National Laboratory, USA.

⁴ Current address: Lawrence Berkeley National Laboratory, USA.

⁵ Current address: Center for Advanced Systems Understanding (CASUS), Germany.



Original Content from this work may be used under the terms of the [Creative Commons Attribution 4.0 licence](https://creativecommons.org/licenses/by/4.0/). Any further distribution of this work must maintain attribution to the author(s) and the title of the work, journal citation and DOI.

quasi mono-energetic ion bunch is produced from thin enough targets [17]. If certain laser and target requirements are met, ion acceleration from thicker targets may have contributions, including hole-boring RPA at the target front, collisionless shock acceleration, and subsequent rear-side TNSA [18]. The resulting energy spectra feature super-elevated dips or even separated quasi mono-energetic proton features [19, 20]. For thin target (surface) layers or transversely small targets, mass limitation can equally cause quasi-monoenergetic ion spectra independent of the acceleration mechanism [10, 11, 21–24] by spatial confinement of the proton source volume to the region responsible for the high-energy tail.

So-called multi-species effects are the result of the ion-ion interaction of varying charge-to-mass constituents during the acceleration phase [25–29]. A momentum exchange arises when two such ion species co-propagate during (or after) acceleration. For the same accelerating fields, ‘lighter’ (q/m) species gain higher velocity, leading to charge separation between both expansion fronts. Additionally, electrostatic repulsion between both species establishes shielding of the heavier species’ ion front inside the rear electron sheath, transferring momentum to mid-energy light ions of the same phase-space region. Those light ions are promoted to higher energies, usually without changing their maximum energy at spectral cutoff.

In a typical proton-acceleration experiment, multiple ion species are present in a thin hydro-carbon contamination layer that inherently covers the target surface. In this case, or when the foil itself is thin enough, light ions quickly outrun the heavier species’ expansion front without significant momentum transfer. This changes with uniformly composed targets. Resulting ion energy spectra exhibit a strong dip of light ions at the cutoff energy of the heavier species (per nucleon) with light ions being accumulated at higher energies [11, 29, 30]. This effect can in turn be combined with a transverse target mass-limitation, enhancing the energies of a significant fraction of target protons [31, 32]. These multi-species effects are quantified using a two-fluid description, e.g. in [4, 30, 33], assuming large ratios between charge-to-mass and density of the two ion species.

In this paper, we systematically characterize the multi-species effect for ultra-short pulse laser interaction with intensities up to the petawatt (PW)-regime. An analytical model that predicts the position of spectral modulation and momentum transfer is presented. Our model is derived for arbitrary density and charge compositions, extending previous models based on rarefaction wave solutions [30, 33] with explicit, scalable inter-species interactions. For a potential experimental realization, we perform a numerical study in foil-like geometry with density and geometric parameters applicable to a novel target system operated with cryogenic gases [34–40]. Contrary to composite targets such as plastics, a homogeneously mixed cryogenic target allows for on-demand tunability of multiple ion species and ratios at solid density [41].

In particular, hydrogen and hydrogen-deuterium (H-D) targets provide the following near-ideal starting conditions: first, only two possible charge states $f_i(0, +1)$ exist in H-D plasmas, yet two ion species with differing charge-to-mass ratio are

present for multi-species effect studies. Potential molecular residues can be omitted at given laser intensities. The operation principle of cryogenic jet targets inhibits the growth of surface contamination layers. Second, with well-known atomic physics of the system and a density of 30 critical densities, a significant portion of the target can be assumed as pre-ionized under realistic laser temporal contrast. Cryogenic H-D jets can be produced with fine-grained control of the mixing ratio while keeping the accumulated ion density constant.

Analytical model In the classical TNSA picture, the front of an ion species expands with $v \sim Z/m$ [6]. Under pre-thermal expansion, the resulting distance between two species’ ion fronts is small compared to the screening scale length at these fronts⁶. Exemplified for hydrogen as light species and heavier deuterium, one can solve Gauss’s law $\partial E/\partial y = \rho/\epsilon_0$ for hydrogen ions in front of the spatial deuterium cutoff (ctf), shielding part of the accelerating field. The rear-side evolution of hydrogen density $n_H(y, t) = n_{0,H} \exp(-y/c_{s,H}t - 1)$ and its electro-static influence upon deuterium ions at cutoff are given as

$$\Delta E_D^{\text{ctf}}(t) = \frac{Z_H q_e}{\epsilon_0} \int_{y_D^{\text{ctf}}}^{y_H^{\text{ctf}}} n_H \cdot dy. \quad (1)$$

Only relevant are the protons between deuterium and hydrogen spatial cutoff at $y_i^{\text{ctf}}(t) \cong c_{s,i}t \cdot [2 \ln(\omega_{p,i}t) + \ln 2 - 3]$ for $\omega_{p,i}t \gg 1$, since charge separation is negligible for small times [6, 42]. Z_i is the ion species’ charge, q_e is the (positive) elementary charge, ϵ_0 is the dielectric constant, $c_{s,i} \approx (Z_i k_B T_e m_i^{-1})^{1/2}$ is the ion acoustic speed of sound, and $\omega_{p,i} = (n_{0,e} Z_i^2 q_e^2 m_i^{-1} \epsilon_0^{-1})^{1/2}$ is the prompt (‘hot’) electron plasma frequency in the rear, scaled for respective ion constants.

We define d as the target deuterium ratio; pure hydrogen targets correspond to $d=0.0$ and pure deuterium to $d=1.0$. Hence, for the total electron density, it follows that $n_{0,e} = Z_D n_{0,D}/d = Z_H n_{0,H}/(1-d) = Z_H n_{0,H} + Z_D n_{0,D}$. Comparing mixed targets to a pure deuterium target, the presence of hydrogen ions leads to a reduced maximum deuterium ion velocity $\Delta v_D^{\text{ctf}}(t)$ at cutoff, correspondingly shifting the deuterium front $y_D^{\text{ctf}}(t)$ by $-\int_0^t \Delta v_D^{\text{ctf}}(t) dt$. This shift leads to additional protons overtaking the slowed down deuterium front which in turn changes $v_D^{\text{ctf}}(t)$. For an estimate of expected deuterium energies in a closed-form expression, one can assume (and we verified this in the simulations) that this additional spatial shift of the deuterium expansion front is small compared to the overall spatial separation between the two ion expansion fronts. This warrants setting the integral term to zero. An inclusion of this effect would be possible by numerically solving the resulting

⁶ The screening length corresponds to the classical Debye length in a thermalized plasma. We checked the validity of our assumption in our PIC simulations. E.g., for $a_0 = 16$ and medium deuterium concentration of $d=0.5$, the screening length at the de-mixed ion front was measured to be increasingly larger than 0.5 m while the distance between the ion fronts was below 1.0 m up to $t^{\text{peak}} \approx 1.7 \tau_{\text{laser}}$.

integro-differential equation of $\Delta v_D^{\text{cf}}(t)$. The following derivation is therefore an upper estimate of expected deuterium energies.

One can integrate the equation of motion $dp_y(t)/dt = Z_D q_e \cdot \Delta E_D^{\text{cf}}(t)$, obtaining

$$\frac{\Delta v_D^{\text{cf}}(t)}{C \cdot \omega_{p,D}^{-1}} = \int_{\omega_{p,D}^{-1}}^t t \left[\left(\frac{e^3}{2\omega_{p,D}^2 t^2} \right)^{m_r} - \frac{e^3}{2\omega_{p,H}^2 t^2} \right] dt \quad (2)$$

with $C = (1-d) \cdot Z_D^{-1} c_{s,H}/e$ (e is Euler's number), $m_r^2 = m_H m_D^{-1}$, and $\tau_D = t \cdot \omega_{p,D}$.

Finally, the cutoff energy K_D^{cf} of the heavier species, which is equal to the spectral position of the modulation in the lighter ion spectrum, can be predicted from a known scaling of the pure $d=1$ case by $K_D^{\text{cf}}(d) = m_D/2 (v_D^{d=1} - \Delta v_D^{\text{cf}})^2$ with

$$\frac{\Delta v_D^{\text{cf}}(\tau_D)}{C} = \frac{e^{3m_r}}{2m_r} \cdot \frac{\tau_D^{2-2m_r} - 1}{2-2m_r} - \frac{Z_D^2 e^3 m_r^2}{Z_H^2 2} \cdot \ln(\tau_D). \quad (3)$$

The energy difference is lost to the lighter species, shifting mid-spectrum protons to higher energies than through regular TNSA. An effective acceleration time should be applied for τ_D . Throughout this paper, the analytical solution in equation (3) will be evaluated with the empirical estimate $\tau_D = 1.3 \cdot \bar{\tau}_L \cdot \omega_{p,D}$ ($\bar{\tau}_L$ is the laser pulse length in seconds) [1].

Following the 1D nature of this model, the spatial density distribution of the hydrogen ions that have already overtaken the deuterium cutoff is not relevant. That assumption is valid along the target-normal as long as no transverse forces displace a significant amount of charge from the axis. With increased deuterium content d in the target, the total number of protons drops accordingly. Deuterium cutoff energies then shift to higher energies since the shielding of rear fields decreases. We obtain a description over arbitrary composition ratios d without a divergence of the predicted energies at $d=1$, contrary to [30, 33].

Our model in equation (3) complements theories for cutoff with signatures visible at significantly higher particle flux in the spectrum. The laser-accelerated, pre-thermal TNSA electron population is characterized via its average kinetic energy $\langle T_e \rangle$ and density n_e^{rear} , as in [6–8]. With the position of the spectral modulation scaling differently with $\langle T_e \rangle$ and n_e^{rear} than the lighter species' cutoff, both quantities of the microscopic electron population can be determined from the same ion energy spectra. Particle-in-cell simulations We verify our model with numerical 2D3V PIConGPU simulations [43, 44]. Operating in a standard regime for many titanium-sapphire (Ti:Sa), ultra-high intensity short pulse laser systems, the explored parameters include those available at the Dresden laser acceleration source ion-acceleration experiment at Helmholtz-Zentrum Dresden—Rossendorf, for its 150 TW and 1 PW stages [45]. The final focusing optics and spot size on target is assumed with $w_{0,I}^{\text{FWHM}} = 3 \mu\text{m}$ [38]. The temporal laser profile is modeled as a Gaussian profile with $\bar{\tau}_I^{\text{FWHM}} = 30\text{fs}$. For the central wavelength of 800 nm we normalize to the critical density $n_c = 1.74 \cdot 10^{21} \text{cm}^{-3}$.

Figure 1 sketches the simulation box, with the laser pulse propagating in a positive y direction. The modeled target is

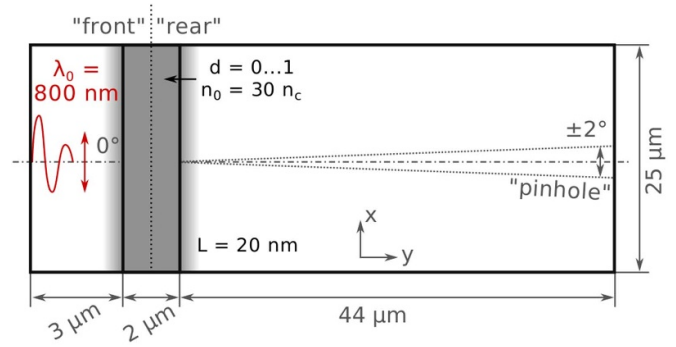


Figure 1. Simulation setup and used naming conventions. *In situ* applied particle filters are modeled according to a pinhole aperture, e.g. in a Thomson parabola. The laser incidence angle is zero degrees (from left along y) and the electric field of the laser pulse is polarized along x .

a planar, cryogenic jet with $2 \mu\text{m}$ thickness, disabling effects of lateral mass limitation [38]. A short exponential ramp with $L=20 \text{nm}$ scale-length was added at the target surface to account for slight hydro-dynamic pre-expansion and increasing numerical robustness.

$$n_e(y) = 30n_c \cdot \begin{cases} e^{-(y-5)/0.02}, & \text{if } y > 5 \\ 1, & \text{if } 3 < y < 5 \\ e^{(y-3)/0.02}, & \text{if } y < 3. \end{cases} \quad (4)$$

Numerical particle-in-cell solvers deployed are the Yee-Maxwell-solver, optimized Esirkepov current deposition (Zig-Zag path splitting), randomized in-cell starting positions without temperature, third order (piecewise cubic) particle assignment shape, Boris particle pusher, and weighted trilinear force interpolation. Collision operators are neglected.

The 2D simulations' spatial resolution is $\Delta x, \Delta y = 3.33 \text{nm}$ with $\Delta t = 7.85\text{as}$ on a grid of 7488×14720 cells. Equivalently, the central laser wavelength is resolved with 240 cells and the non-relativistic plasma frequency with $\omega_{p,e} \cdot \Delta t = 0.1$. Per ion species, 20 particles per cell and one electron particle per ion are initialized as pre-ionized macro-particle distribution. Each simulation computes approximately 0.6ps interaction time on 16 GPUs (Nvidia P100) within 1:20–1:45 hours.

Peak laser intensities on target are varied in steps of the dimensionless field amplitude $a_0 = 8, 16, 23, 30$, and 42. The laser pulse propagates in the positive y direction, while the focal position is set to the target center at $4 \mu\text{m}$. For detailed analysis, a radial particle acceptance filter is deployed, similar to realistic experimental pinhole apertures with $\pm 2^\circ$. Additionally, particles originating in the first half of the target, $y_0 \leq 4 \mu\text{m}$, are tracked as target 'front' and all other particles as target 'rear' for discussion. Further numerical parameters of our simulations, open source code, and scripts are described in the supplementary material.

Figure 2 summarizes the resulting ion spectra for $a_0 = 16$. An overall exponential shape confirms operation in the TNSA

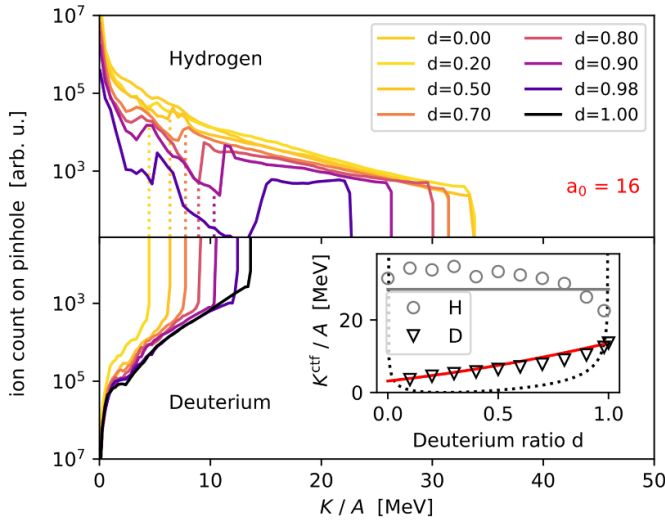


Figure 2. Deuterium and hydrogen energy spectra for $a_0 = 16$ for variations in target deuterium ratio d . The inset displays ion cutoff energies for variations of d . Our analytical model from equation (3) is plotted as a red line and a gray line for reference [6] equation (22), both with measured average $\langle T_e \rangle = 2.17$ MeV and $n_e^{\text{rear}} = 0.31 \cdot n_{0,e}$. The dotted black line is a previous model for the heavy species cutoff energy in [30, 33] equation (1).

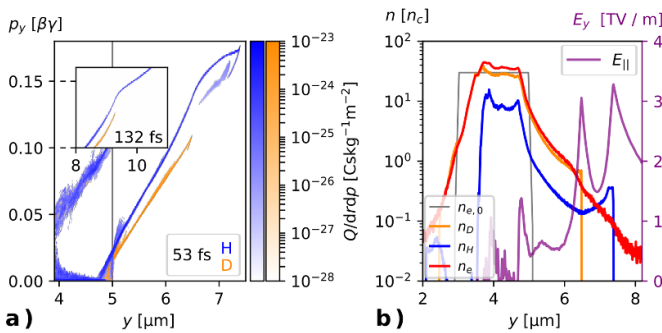


Figure 3. (a) Longitudinal phase space for $a_0 = 16$ for a deuterium ratio $d = 80\%$. Taken at time $t = 53$ fs after the peak intensity of the laser pulse reached the target. The inset shows the rear ion evolution at $t = 132$ fs. (b) Fields shown for same time. Clearly visible is the partial shielding of the electron sheath through expanding protons around $7 \mu\text{m}$. The bump of proton density at its front originates from the initial rear scale length [6].

regime [6]. The deep modulation of the proton spectra corresponds to the cutoff energy per nucleon of the heavier deuterium species; the latter we predict with our model from equation (3). For the same measured average electron kinetic energy $\langle T_e \rangle$ and density n_e^{rear} , the theoretical predictions for proton cutoff (gray line) and deuterium cutoff (red line) are added. For $d \rightarrow 1$, quasi-monoenergetic features are formed in the lighter species.

A phase space image in figure 3(a) shows that hydrogen ions expand faster from the target rear side than deuterium, which is consistent with TNSA scalings for the ion front velocity applied in equation (1). The deuterium front therefore interacts dominantly with protons in the mid-range of the spectrum, which are shifted longitudinally to higher energies due to

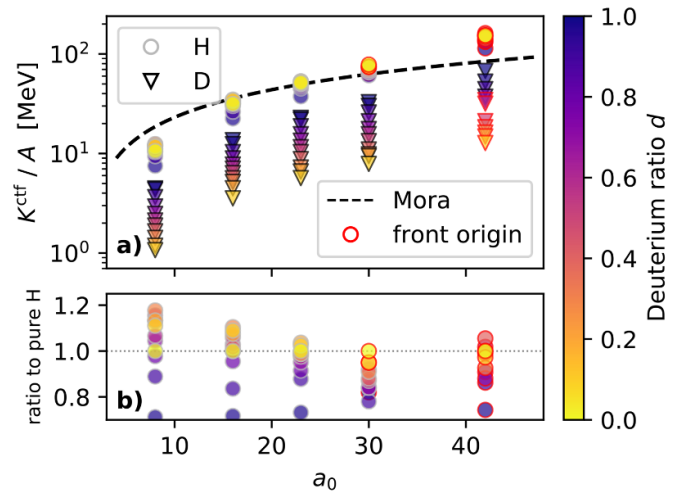


Figure 4. (a) Deuterium (triangle) and hydrogen (sphere) cutoff energies with varying laser intensity. For a given a_0 , each H-D pair with the same deuterium ratio d (color) corresponds to one simulation. The dashed line is a simple estimate for Mora scaling [6] with constant $n_e^{\text{rear}} = 0.35$ and $\langle T_e \rangle$, as in [8]. (b) Zoomed plot for hydrogen cutoff energies: relative energy increase/decrease compared to a pure hydrogen target ($d = 0$) under variation of deuterium content d . The variation of target composition leads to enhancements up to 18% and reduction of 28% in hydrogen cutoff energy, respectively.

electro-static repulsion. A lineout in figure 3(b) shows the resulting modulated proton density and the peaked electric field (purple) at each ion species' front at a later time.

Integrating the overall proton signal in 'pinhole' acceptance reveals that the on-axis spectrum is indeed solely pushed to higher energies and deuterium-caused 'loss' of protons on-axis due to transverse displacement is negligible. Consistently, the spectral hydrogen accumulation after each dip in figure 2 consists of the protons in the dip. However, by keeping the initial target density constant with mixing ratios d , proton counts for mid-spectrum energies do not exceed values of the pure hydrogen case.

As we vary the laser intensity on target in figure 4(a), the proton cutoff energy increases with a_0 due to increasing electro-static TNSA field strengths, driven predominantly by prompt, laser-accelerated electrons. The increase of deuterium cutoff energy with deuterium mixing ratio d holds true, even for PW-scale laser intensities.

Even in TNSA, the highest energy can be acquired by front-side originating ions for $a_0 \gtrsim 30$, which are indicated by red marker edges in figure 4. While the initial hole-boring velocity for ions at the target front surface increases with a_0 (kinetic energy of protons $K_{\text{HB}} = 0.26 - 6.0$ MeV) [46], their final kinetic energy is dominated by acceleration in the rear-side TNSA fields [19, 20]. For $a_0 \gtrsim 30$, front-side ions are fast enough to experience strong, continued acceleration in TNSA rear fields, in which they reach even higher energies than rear-side ions that need to be accelerated from zero velocity. At the given target thickness, this does not occur at lower a_0 because, there, front-originating ions do not reach the transient TNSA fields at the expanding target rear to be post-accelerated.

For the target thickness studied here ($2\ \mu\text{m}$), we observe that the multi-species spectral modulation becomes less pronounced with higher intensity (additional figures are in the appendix, figure C1). This is a clear indication that the observed acceleration regime is not light-sail RPA-dominated, where proton acceleration from ultra-thin ($\lesssim 100\ \text{nm}$) targets can result in narrower energy spectra with increasing laser intensity [19].

Calculation of the relativistic skin depth $c/\omega_{p,e}^{\text{rear}} = 98\ \text{nm}$ suggests that a $2\ \mu\text{m}$ thick, $30 n_c$ target remains opaque even for the highest $a_0 = 42$ (average relativistic gamma factor for electrons is $\gamma_e^{\text{rear}} = 17.9$). However, the hole-boring front burns through the target before the end of the laser intra-pulse phase for $a_0 \gtrsim 20$, resulting in the observation of transmitted light. Field lineouts are shown in figure E4 in the supplementary material.

This study is performed with an overall conserved target free-electron density. In the TNSA regime with thick targets, deuterium ions only modulate mid-energy protons, and the cutoff energy for protons for a constant a_0 would be expected to be independent of d , hence we plot a constant prediction for Mora scaling in figure 2. Intriguingly, our simulations as well as data in previous studies show a monotonically decreasing cutoff energy with proton density [11]. Furthermore, we observe a slight increase (up to 18%) in proton cutoff energy compared to pure hydrogen targets, detailed in the linear plot of figure 4(b). This secondary effect is likely attributed to slightly changed absorption efficiency on the target front – for example, due to micro-structuring of the surface – as we measure a change in average electron energy density (refer to the supplementary material for details).

Conclusions In summary, we developed an analytical model for the multi-species effect, predicting the reduced cutoff energy of a heavier ion species and associated position of spectral modulations for arbitrarily mixed, homogeneous composite targets in planar geometry. We calibrated our model against the cutoff energy of a target consisting purely of the heavier species, which can be either measured, simulated or derived from established theories [6, 8, 47].

Combining our results for spectral modulations with models for proton cutoff energy offers advanced predictive capabilities for properties of the laser-driven electron population. In particular, average electron kinetic energy and density assumptions can be self-consistently verified against both cutoff and modulation in the lighter ion species' energy spectra.

We performed 60 systematic *ab initio* simulations on multi-species effects for a planar, homogeneous cryogenic target, irradiated with PW-scale laser intensities. Spectral signatures observed in our simulations are unique to multi-species effects and exhibit striking agreement with analytic predictions. A deuterium-hydrogen jet target was investigated in view of a methodical experimental realization, as its operation principle provides easy control over the target constituents and inhibits surface contamination, thus limiting the available charge states and simplifying ionization physics. Thus, this target offers the unique opportunity to study multi-species effects at variable

target composition in a well-defined environment. However, our model is open to in-detail adjustments of individual starting conditions of laser and target parameters in view of many different experimental situations, as well as uncertainties and adjustments of specific numerical models used, e.g. for ionization or collisions.

The presented analytical model in equation (3) is not limited to the H-D jets addressed in this study. Adaption to other target constituents with different charge-to-mass ratios is straightforward. In fact, virtually all ion-acceleration schemes at ultra-high laser intensities have relevant contributions from multi-species effects even for pure materials, where different ionization states take the role of the different ion species addressed in this work.

Acknowledgments

The work has been partially supported by EC H2020 Laserlab Europe V (PRISES), contract no. 871124. This project received funding within the MEPHISTO project (BMBF-Förderkennzeichen 01IH16006C). Computations were performed on the Hemera cluster at Helmholtz-Zentrum Dresden—Rossendorf. We acknowledge all contributors to the open-source code PIConGPU for enabling our simulations. We thank all contributors to the SciPy ecosystem for enabling our data analysis. We thank F Fiuza, S Göde, Y Long, and L Huang for fruitful discussions. Figures 1–C1, D3, E4(a), and F5 are adopted from reference [48] under CC-BY-SA-4.0 license.

Appendix A. Data availability

Simulation input files, in situ analysis output, scripts and analyzed data that support the figures and other findings of this study are available from DOI:10.14278/rodare.116.

PIConGPU is open source and all versions, including 0.4.3 used in this paper, are available for download and as a contributable git repository [43, 44].

Additional high-resolution, raw HDF5 files using the open-PMD standard (DOI:10.5281/zenodo.1167843) increase simulation output data to 4.7 TByte and are available from the corresponding author upon reasonable request.

Appendix B. Simulation time

The laser pulse's peak intensity reaches the target after 8190 steps (64.3 fs). Energy spectra were compared on final, converged results before particles leave the simulation box, at step 90 000, 75 000, 70 000, 60 000 or 45 000, depending on laser intensity.

Appendix C. Simulation and analytical results for $a_0 = 8, 23, 30, 42$

The explicit form of the prediction for the heavier species' cutoff energy in equation (3) is:

$$K_D^{\text{ctf}}(d, \langle T_e \rangle) = \frac{m_D}{2} \cdot \left[\sqrt{K_D^{d=1, \text{ctf}} \cdot \frac{2A_D}{m_D} - \frac{(1-d)}{\epsilon \cdot Z_D} \sqrt{\frac{Z_H k_B \langle T_e \rangle}{m_H}}} \right. \\ \left. \left(\frac{\epsilon^{3m_r}}{2^{m_r}} \cdot \frac{\tau_D^{2-2m_r} - 1}{2-2m_r} - \frac{Z_D^2}{Z_H^2} \frac{\epsilon^3 m_r^2}{2} \cdot \ln(\tau_D) \right) \right]^2. \quad (5)$$

All quantities are given in SI, ϵ is Euler's number, $m_r^2 = m_H m_D^{-1}$ and $\tau_D = t \cdot \omega_{p,D}^{d=1} \approx 1.3 \cdot \bar{\tau}_L \cdot \omega_{p,D}^{d=1}$ are unitless [1].

Replacing Z_D, A_D, m_D for any other heavy ion species or choosing another 'light' ion species for the same quantities in X_H variables should hold true and no assumptions over the abundance or ratio between the two are taken into the derivation. Note to readers: previous papers [30, 33] annotated quantities X_H for 'heavy' and X_L for 'light' ions. Our choice of H of the light hydrogen (proton) species is the exact opposite. Translating [30, 33] equation (1) in our nomenclature reads

$$K_D^{\text{ctf}} = Z_D \langle T_e \rangle \ln^2 \left[4Z_D d \sqrt{2A_D Z_H / A_H Z_D} / (Z_H (d-1) \epsilon) \right] / 2 \quad (6)$$

$$K_H^{\text{peak}} = Z_H \langle T_e \rangle \ln \left[4Z_D d \sqrt{2A_D Z_H / A_H Z_D} / (Z_H (d-1) \epsilon) \right]. \quad (7)$$

In our model, we derive the cutoff energy K_D^{ctf} of the heavier species. As the lighter species is shifted to higher energies from this spectral position, a peak is observed at K_H^{peak} for protons. Previous models described this as in equation (7). Our new model is compared against equation (6) as a black dotted line in figures 2 and C1.

Figure C1 provides additional energy spectra collections for various simulated laser intensities of the main text. Averaged kinetic energies $\langle T_e \rangle$ and n_e^{rear} are a best-effort to measure in situ from simulation data. Please see a summary of the method below and the provided scripts for its implementation. Further mathematical and algorithmic details are described in appendix 3 of [48]. Alternatively, like previous authors, one could apply a theoretical scaling for the average kinetic energy, such as [8], and approximate $n_e^{\text{rear}} \approx n_0 \cdot \eta$ via the absorption in figure D2.

Appendix D. Determination of $\langle T_e \rangle$ and n_e^{rear}

Figure D2 shows the relative ratio of laser energy absorbed by the target.

In order to estimate the average kinetic energy $\langle T_e \rangle$ and n_e^{rear} for electrons in simulations, various methods are used in contemporary literature, yet rarely documented. Either apply one of the theoretical models for $\langle T_e \rangle$, such as [8], and assume the all-target absorption $\eta \approx n_e^{\text{rear}} / n_{0,e}$ or try to measure in situ, as shown in figure D3.

In our analysis of electrons in the simulation, we select a spatial region around the laser axis in the second half of the target and measure the prompt, laser-accelerated electrons with relativistic values for γ_e . We measure shortly after the laser

peak intensity reaches the target. The resulting average kinetic energy and density is then corrected for the missing low-energy contribution due to our spectral γ_e -cutoff, assuming a Boltzmann distribution, which we verify in electron energy histograms for the assumed 'prompt' selection.

We observe deviations from those predictions at $a_0 = 8$ and 42. Comparing theoretical predictions for hydrogen cutoff energy for $a_0 = 8$, we realize our selection of prompt electrons underestimates the electron density relevant for acceleration of ions. We therefore included a fraction of bulk electrons in this specific measurement in order to account for re-heating effects and slow expansion, which is influenced by non-prompt electrons at this low intensity. Nevertheless, this method of measurement likely underestimates the average kinetic energy of electrons due to crude averaging of both bulk and prompt electron distributions. Due to burn-through of the target for the $a_0 = 42$ case, the laser can penetrate the target and electrons can co-propagate with its phase, increasing the average electron energy above the case of a solid, reflecting surface, and therefore values exceed the dashed black line, showing [8] equation (9).

Observing the energy-density of laser-accelerated electrons in figure D3 (red data points), a maximum is achieved for a deuterium ratio of about $d = 20\text{--}50\%$ for $a_0 < 20$. Following [6], this translates into a maximum acceleration field and hence maximum proton energies (gray data points).

We therefore conclude that the deuterium ratio in the target modifies the front-side absorption of the laser energy into Debye sheath electrons. Since we do not observe a correlated change in the front-side plasma steepness, this change in absorption is likely due to varied micro-structuring of the surface or other 2D effects.

Appendix E. Target rear

Figure E4(a) exemplifies the electric field on the target rear. Clearly visible is the $2\omega_0$ imprinting of the laser frequency onto the rear-side, promptly accelerated electrons. From comparisons between different deuterium ratios d , we find that an optimal absorption of laser energy into maximum number of electrons on the target rear ($y > 5.0 \mu\text{m}$) and maximum accelerating field can be designed with about 20%–50% deuterium in the target. This leads to cutoff energy increase for $a_0 = 8 - 16$ of up to 18% compared to a pure proton target of the same density.

Figure E4(b) demonstrates that the target stays locally opaque even for $a_0 = 42$ during laser interaction: note the section at $y = 4 - 6 \mu\text{m}$ on which the electron density (red) is larger than the relativistic critical density (black). Nevertheless, plasma filaments are observed breaking up transverse sections of the target, enabling burn-through.

Appendix F. Ion emission distribution

Figure F5 shows the angular energy emission distribution in the laser pulse polarization direction. When comparing ion

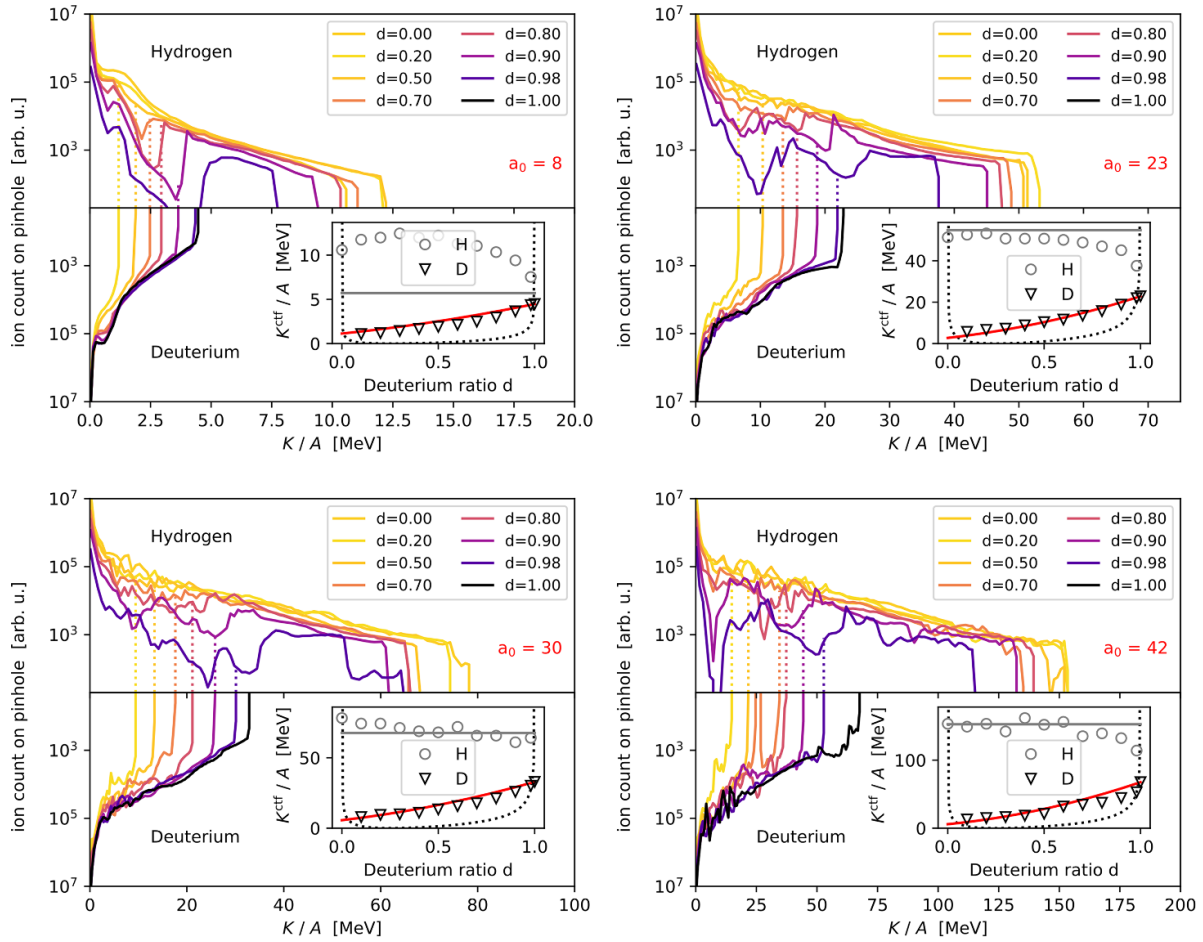


Figure C1. Deuterium and hydrogen energy spectra for laser strengths parameter $a_0 = 8 - 42$. Individually shown as in figure 2 for variations in target deuterium ratio d . Ions shown for ± 2 degree ‘pinhole’ acceptance. In the insets, the theoretical prediction from equation (3) is presented as a red solid line and the hydrogen cutoff following Mora scaling as a gray line [6] for $\langle T_e \rangle = (0.35, 3.52, 4.52, 8.64)$ MeV and non-perfect absorption into rear electrons $n_e^{\text{rear}} = (0.48, 0.44, 0.40, 0.57) \cdot n_{0,e}$ for $a_0 = (9, 23, 30, 42)$. The dotted back line is from a prior model for the heavy species cutoff energy from equation (6).

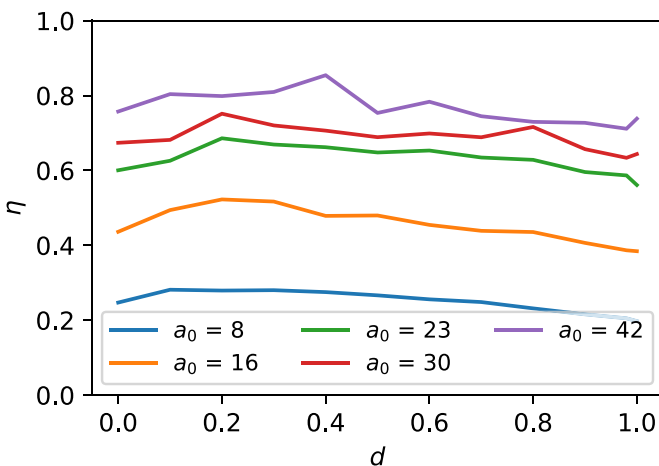


Figure D2. Energy conversion η from laser energy to kinetic particle energy over laser strength parameter a_0 and relative deuterium content d .

pointing for varying laser intensities, both hydrogen and deuterium emission distributions are more directed for low a_0 than higher a_0 . In our setup, front-side protons add a diffuse

emission signature on top of the rear-side, directed protons due to hole-boring RPA contributions. The emission characteristics of hole-boring pre-accelerated ions from the target front surface (e.g. wider or narrower than the TNSA rear and structuring) depends on the given laser contrast and target pre-expansion and requires a detailed parameter scan for a given experiment. In our specific setup, front-side contributions emit into wider angles than rear-side ions. Note that the absolute values for energy and emission angle will both be smaller in 3D3V simulations and experiments; an experimental identification for areas of pure front-side contributions might be possible when clear structural changes are visible.

With increasing deuterium content in the target, the visible ‘hole’ (marked red in figure F5) in mid-range protons shifts to higher energies as more deuterium ions can displace the decreasing number of protons more efficiently. Experiments will observe a ‘gap’ at low energies and quasi-monoenergetic features when observing strictly along the target-normal with narrow angle acceptance. Under limited cryogenic target orientation stability [38], such measurements might suffer from shot-to-shot fluctuation of target-normal alignment with respect to the fixed diagnostic axis. The lineouts on the right

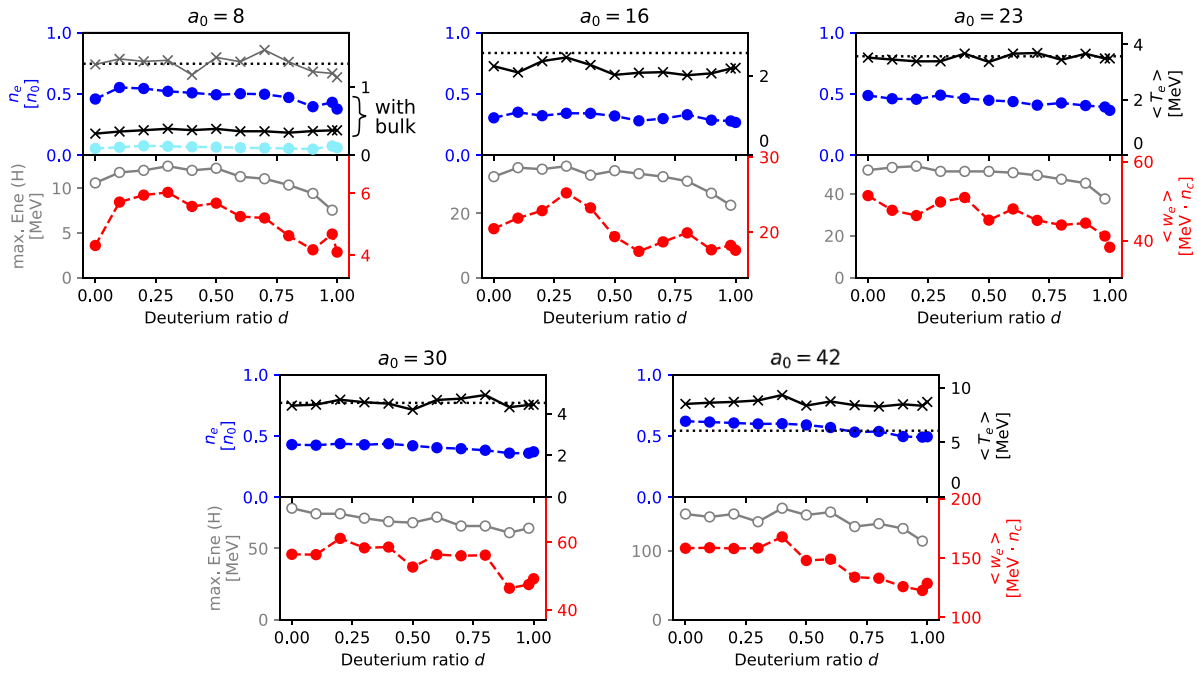


Figure D3. In situ measured parameters for laser-accelerated electrons: density ratio to cold target n_e (blue), average kinetic energy $\langle T_e \rangle$ (black), resulting average energy density $\langle w_e \rangle$ (red) versus hydrogen cutoff energy (gray). The black dashed line is the theoretical scaling on $\langle T_e \rangle$ from [8] equation (9).

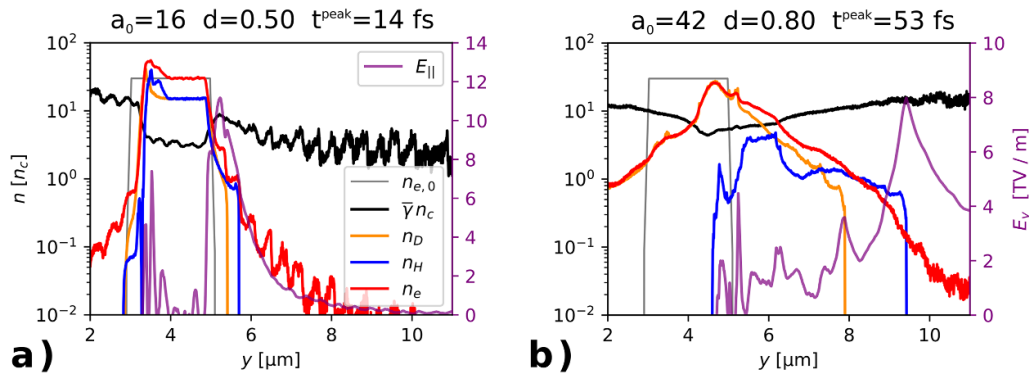


Figure E4. Lineouts of plasma density and longitudinal electric field at an early stage of the acceleration. a) $a_0 = 16$ and target deuterium ratio $d = 0.5$. b) $a_0 = 42$ and target deuterium ratio $d = 0.8$.

side of each plot in figure F5 exemplify how a positioning jitter of 7° ($a_0 = 16$) influences the measured spectra. Experimental campaigns can mitigate this issue by either collecting enough statistics or deploying wider, angle-resolved spectrometers (resolution $\leq 10^\circ$).

Appendix G. In-target origin of energetic ions

For TNSA, the highest accelerating fields are expected at the rear surface of the target. Figure G6 connects the initial target depth of a hydrogen ion with its finally reached energy. On the right of each figure, the forward-observed proton spectrum (red) with a blue line showing rear and green line showing front-side contributions corresponds to the integral over the initial target depth.

Over increased a_0 , the influence of front-side originating ions onto spectral modulations increases and finally dominates the cutoff energy for the PW-scale $a_0 = 42$. Front-side ions are further accelerated in the rear electro-static fields, which unsurprisingly leads to a similar spectral shape.

For an investigated a_0 of 30 and above, a deuterium ratio of 90% is required to cause a significant modulation in the proton spectra. Accelerating rear fields scale with laser strengths from increased sheath electron energy. However, the superimposed multi-species fields that cause the spectral modulation do not increase with a_0 and depend on target composition.

Not only do rear-surface protons experience a modulation, but also front-side, hole-boring RPA-influenced protons are affected by deuterium ions [13]. Further details are shown in figure H7.

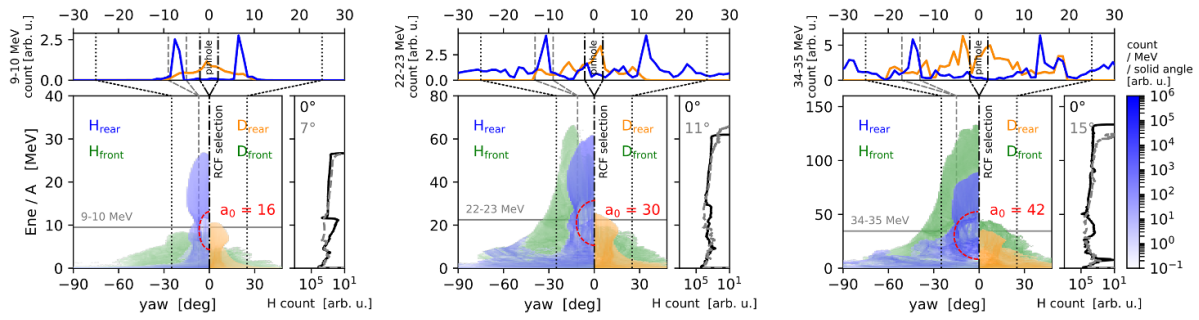


Figure F5. Lower plots: emission distribution of ions. Plotted for laser intensities $a_0 = 16, 30, 42$ (left–right) and target deuterium ratio $d = 90\%$. Left half is hydrogen (blue) and right half is deuterium ions (orange) with green denoting front-originating ions in both cases. For a large enough angle to the laser axis and energy, one can infer that only front-side ions contribute (areas plotted solely in green). Rear-side ions are plotted on top of front-side ions. Upper plots: A sample lineout, zoomed into a forward direction, shows emission characteristics for a selected energy ($\Delta Ene/A = 1$ MeV), similar to a radiochromic film layer (summed over front and rear contributions). Side plots on right: Energy lineout for pointing sensitivity with a pinhole aperture taken for acceptance on axis (black line: $(0 \pm 2)^\circ$) and off-axis ($(7, 11, 15 \pm 2)^\circ$), similar to a typical Thomson parabola.

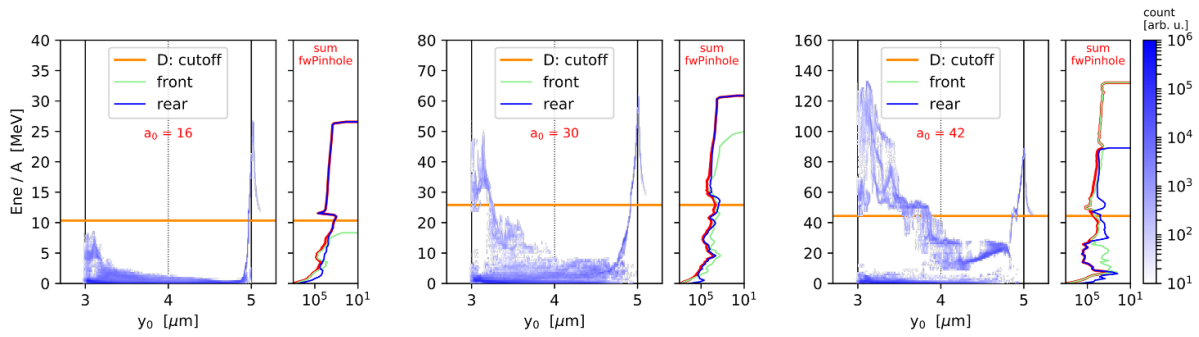


Figure G6. Correlation of final energy depending on initial longitudinal position y_0 inside the target for hydrogen ions. Plotted for laser intensities $a_0 = 16, 30, 42$ and target deuterium ratio $d = 90\%$. y_0 describes the target along the laser-axis (laser from left); target front and rear are defined as initial position y_0 before or after $4 \mu\text{m}$. Lines on the right show individual contributions of front (first micron up to $y_0 = 4 \mu\text{m}$ in the target) and rear ions on the observed energy spectra in ‘forward pinhole’ acceptance.

For $a_0 \gtrsim 30$, at energies in the spectrum above the cutoff of rear-side ions, one might expect a change in slope in the overall proton spectra as front-side ions start to dominate the highest energies (red line in figure G6). In some cases, a small energy modulation hints at the change between the front and rear contributions, which might not be significantly observable, since front-side ions are also pre-dominantly further accelerated in TNSA fields. As this is the observable obtained in an experiment, it is not possible to quickly infer which part of the spectrum is front- or rear-side originated without further radial emission information.

Appendix H. Multi-species effect on front-side ions for $a_0 = 42$

Figure H7 (top) shows a correlation plot between the original in-target position and final energy of hydrogen ions for case $a_0 = 42$. For the high-deuterium case $d = 0.8$, front-side originating ions are equally affected by the multi-species effect from deuterium (see orange line for deuterium cutoff energy). The reason for that lies in the sufficiently long co-propagation through the target after initial front-side hole-boring acceleration. The longitudinal phase-space plots

(bottom) show once again the proximity of deuterium and hydrogen ions as they are still within the target during burn-through, 14 fs after peak laser intensity on target.

Appendix I. Notes for potential experimental realizations

For significant energy modulation signatures in the high-energy tail of distributions, a deuterium ratio $\geq 60\%$ is advisable. The observed multi-species effects are rather robust against small changes in deuterium ratio. Therefore, the mixing ratio only needs to be generated with a precision of a few percent. Additionally, we observed an increase of proton cutoff energies in simulations for mixing ratios between 20% and 50%.

For spectrometer setups, an energy resolution for the mid-energy range needs to be chosen that can resolve the few-MeV wide energy modulation. When deciding for an ion spectrometer with high energy resolution but small angular acceptance, such as a Thomson parabola, a statistically significant amount of shots needs to be accumulated in case the target orientation jitter obfuscates the otherwise clear signature in the energy spectrum of target-normal directed protons. The

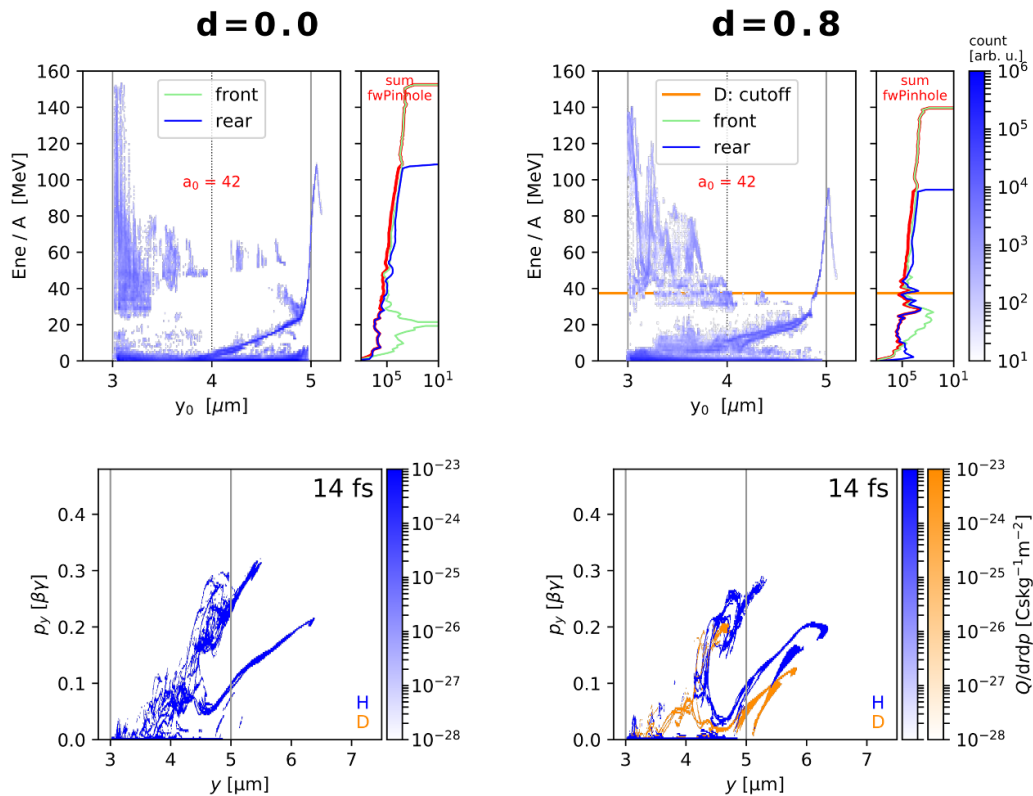


Figure H7. Multi-species effect for front-side ions for $a_0 = 42$, comparing a pure hydrogen target ($d = 0.0$, left column) and a mixed target ($d = 0.80$, right column). Selected plots show particles in acceptance for a ‘forward pinhole’. Upper plots: origin of final energies for hydrogen ions. Lower plots: longitudinal phase space for early times, 14 fs after laser peak intensity on target.

dynamic range in terms of proton counts per energy and solid angle should at least be three orders of magnitude for a good resolution of the start and end of the modulation.

ORCID iDs

Axel Huebl <https://orcid.org/0000-0003-1943-7141>
 Martin Rehwald <https://orcid.org/0000-0001-6200-6406>
 Lieselotte Obst-Huebl <https://orcid.org/0000-0001-9236-8037>
 Tim Ziegler <https://orcid.org/0000-0002-3727-7017>
 Marco Garten <https://orcid.org/0000-0001-6994-2475>
 René Widera <https://orcid.org/0000-0003-1642-0459>
 Karl Zeil <https://orcid.org/0000-0003-3926-409X>
 Thomas E Cowan <https://orcid.org/0000-0002-5845-000X>
 Michael Bussmann <https://orcid.org/0000-0002-8258-3881>
 Ulrich Schramm <https://orcid.org/0000-0003-0390-7671>
 Thomas Kluge <https://orcid.org/0000-0003-4861-5584>

References

- [1] Fuchs J *et al* 2006 *Nat. Phys.* **2** 48–54
- [2] Wilks S C *et al* 2001 *Phys. Plasmas* **8** 542
- [3] Zeil K *et al* 2010 *New J. Phys.* **12** 45015
- [4] Gurevich A V, Pariiskaya L V and Pitaevskii L P 1973 *JETP* **36** 274
- [5] Denavit J 1979 *Phys. Fluids* **22** 1384
- [6] Mora P 2003 *Phys. Rev. Lett.* **90** 185002
- [7] Zeil K, Metzkes J, Kluge T, Bussmann M, Cowan T E, Kraft S D and Sauerbrey R 2012 *Nat. Commun.* **3** 874
- [8] Kluge T, Cowan T, Debus A, Schramm U, Zeil K and Bussmann M 2011 *Phys. Rev. Lett.* **107** 205003
- [9] Ditmire T, Tisch J W G, Springate E, Mason M B, Hay N, Smith R A, Marangos J and Hutchinson M H R 1997 *Nature* **386** 54
- [10] Hegelich M *et al* 2002 *Phys. Rev. Lett.*
- [11] Robinson A P, Bell A R and Kingham R J 2006 *Phys. Rev. Lett.* **96** 035005
- [12] Steinke S *et al* 2013 *Phys. Rev. Spec. Top.—Accelerators Beams* **16** 011303
- [13] Kar S *et al* 2012 *Phys. Rev. Lett.* **109** 185006
- [14] Sokollik T *et al* 2008 *Appl. Phys. Lett.* **92** 091503
- [15] Quinn K *et al* 2009 *Phys. Rev. Lett.* **102** 194801
- [16] Masood U, Bussmann M, Cowan T E, Enghardt W, Karsch L, Kroll F, Schramm U and Pawelke J 2014 *Appl. Phys. B* **117** 41–52
- [17] Macchi A, Veghini S and Pegoraro F 2009 *Phys. Rev. Lett.* **103** 085003
- [18] Macchi A, Borghesi M and Passoni M 2013 *Rev. Mod. Phys.* **85** 751
- [19] Qiao B, Kar S, Geissler M, Gibbon P, Zepf M and Borghesi M 2012 *Phys. Rev. Lett.* **108** 115002
- [20] Higginson A *et al* 2018 *Nat. Commun.* **9** 724
- [21] Bulanov S V, Esirkepov T Z, Kamenets F F, Kato Y, Kuznetsov A V, Nishihara K, Pegoraro F, Tajima T and Khoroshkov V S 2002 *Plasma Phys. Rep.* **28** 975
- [22] Esirkepov T *et al* 2002 *Phys. Rev. Lett.* **89** 175003
- [23] Pfothenauer S M 2008 *New J. Phys.* **10** 033034
- [24] Zeil K *et al* 2014 *Plasma Phys. Control. Fusion* **56** 084004

- [25] Joshi C, Richardson M C and Enright G D 1979 *Appl. Phys. Lett.* **34** 625
- [26] Begay F and Forslund D W 1982 *Phys. Fluids* **25** 1675
- [27] Allen M *et al* 2003 *Phys. Plasmas* **10** 3283
- [28] Kemp A J and Ruhl H 2005 *Phys. Plasmas* **12** 033105
- [29] Psikal J, Tikhonchuk V T, Limpouch J, Andreev A A and Brantov A V 2008 *Phys. Plasmas* **15** 053102
- [30] Tikhonchuk V T, Andreev A A, Bochkarev S G and Bychenkov V Y 2005 *Plasma Physics and Controlled Fusion* **47** B869
- [31] Kluge T, Enghardt W, Kraft S D, Schramm U, Zeil K, Cowan T E and Bussmann M 2010 *Phys. Plasmas* **17** 123103
- [32] Hilz P *et al* 2018 *Nat. Commun.* **9** 423
- [33] Brantov A V, Tikhonchuk V T, Klimo O, Romanov D V, Ter-Avetisyan S, Schnürer M, Sokollik T and Nickles P V 2006 *Phys. Plasmas* **13** 122705
- [34] Garcia S, Chatain D and Perin J P 2014 *Laser Part. Beams* **32** 569–75
- [35] Margarone D *et al* 2016 *Phys. Rev. X* **6** 041030
- [36] Göde S *et al* 2017 *Phys. Rev. Lett.* **118** 194801
- [37] Kraft S D *et al* 2018 *Plasma Phys. Control. Fusion* **60** 044010
- [38] Obst L *et al* 2017 *Sci. Rep.* **7** 10248
- [39] Obst-Huebl L *et al* 2018 *Nat. Commun.* **9** 5292
- [40] Scott G G *et al* 2018 *Phys. Rev. Lett.* **120** 204801
- [41] Kim J B, Schoenwaelder C and Glenzer S H 2018 *Rev. Sci. Instrum.* **89** 10K105
- [42] Allen J E and Andrews J G 1970 *J. Plasma Phys.* **4** 187–94
- [43] Bussmann M *et al* 2013 SC '13: Proc. Int. Conf. High Performance Computing, Networking, Storage and Analysis p 5
- [44] Huebl A *et al* 2019 *PICongPU 0.4.3: System Updates and Bug Fixes* (<https://doi.org/10.5281/zenodo.2565503>)
- [45] Schramm U *et al* 2017 *J. Phys.: Conf. Series* **874** 012028
- [46] Robinson A P, Gibbon P, Zepf M, Kar S, Evans R G and Bellei C 2009 *Plasma Phys. Control. Fusion* **51** 024004
- [47] Schreiber J *et al* 2006 *Phys. Rev. Lett.* **97** 045005
- [48] Huebl A 2019 PICongPU: predictive simulations of laser-particle accelerators with manycore hardware *PhD Thesis* Technische Universität Dresden (<https://doi.org/10.5281/zenodo.3266820>)